Dynamics and conductivity near quantum criticality

Snir Gazit,[1] Daniel Podolsky,[1] Assa Auerbach,[1] and Daniel P. Arovas[2]

[1]*Physics Department, Technion, 32000 Haifa, Israel*

[2]*Department of Physics, University of California at San Diego, La Jolla, California 92093, USA*

Relativistic O(N) field theories are studied near the quantum-critical point in two space dimensions. We compute dynamical correlations by large-scale Monte Carlo simulations and numerical analytic continuation. In the ordered side, the scalar spectral function exhibits a universal peak at the Higgs mass. For $N = 3$ and 4, we confirm its ω^3 rise at low frequency. On the disordered side, the spectral function exhibits a sharp gap. For $N = 2$, the dynamical conductivity rises above a threshold at the Higgs mass (density gap), in the superfluid (Mott insulator) phase. For charged bosons (Josephson arrays), the power-law rise above the Higgs mass increases from two to four. Approximate charge-vortex duality is reflected in the ratio of imaginary conductivities on either side of the transition. We determine the critical conductivity to be $\sigma_c^* = 0.3(\pm 0.1) \times 4e^2/h$ and describe a generalization of the worm algorithm to $N > 2$. We use a singular value decomposition error analysis for the numerical analytic continuation.

I. INTRODUCTION

Relativistic O(N) models describe the low-temperature properties of diverse condensed matter systems, e.g., quantum antiferromagnets, charge density waves, Josephson junction arrays, granular superconductors, and Bose condensates in optical lattices.[1–3] Many of these systems exhibit a quantum phase transition, as a function of a tuning parameter, between phases where the O(N) symmetry is present and where it is spontaneously broken.

Far from criticality, the collective excitations in these systems are well understood. In the symmetric phase, there are N massive modes. In the broken symmetry phase, there are $N - 1$ massless Goldstone modes and one massive amplitude (Higgs) mode.[4] The Higgs is actually a resonance since it can decay into pairs of Goldstone modes. The shape of the resonance in two spatial dimensions has recently attracted significant theoretical and experimental interest. Weak coupling and $N = \infty$ diagrammatic expansions[5,6] have shown that a careful choice of the correlation function ensures that the Higgs mode can be detected, without spurious contamination from massless Goldstone modes. Indeed, the Higgs resonance has been directly observed in recent experiments of the Mott insulator to superfluid transition in optical lattices.[7]

Near the quantum-critical point (QCP), the dynamics in two spatial dimensions is determined by a strongly coupled fixed point, thus precluding a simple description in terms of weakly interacting quasiparticles. In the ordered phase, Goldstone's theorem still ensures the existence of Goldstone modes, which are long lived at low energy. By contrast, there is no corresponding protection for the Higgs mode. A $1/N$ expansion of the scalar susceptibility[8] and numerical quantum Monte Carlo (QMC) simulations[9] provided the first evidence for the survival of the Higgs near criticality. Although the low-frequency spectral function near criticality is predicted to be universal,[4,8] its determination requires numerical computation. Recently, this was undertaken by large-scale QMC simulations of the scalar susceptibility for the O(2) and O(3) models[10] and for the Bose-Hubbard model.[11] The Higgs peak in the ordered phase was clearly identified.

In this paper, we further study the dynamical properties of relativistic O(N) models close to the quantum-critical point at low temperature, frequency, and zero wave vector. We review in detail our previous work in which we computed the universal line shape of the scalar susceptibility[10] and present new numerical results for O(N) models with $N = 2$, 3, and 4. In particular, we perform a careful analysis of the low-frequency behavior of the line shape in the ordered phase, where we confirm the ω^3 rise for $N = 3$ and 4 predicted in Ref. 5. For $N = 2$, we can not resolve the low-frequency power law. The scalar response in the disordered phase exhibits a sharp threshold above a gap.

We present new results for the dynamical conductivity of the O(2) model on both sides of the transition. In the superfluid phase, we find a thresholdlike behavior in the conductivity, which rises quadratically with frequency above the Higgs mass m_H. In the insulator, there is a low-frequency threshold in the conductivity appearing at twice the single-particle gap Δ, and a negative (capacitive) linear dependence of the imaginary conductivity.

Throughout the analysis we identify a number of universal constants that characterize the critical point. These include ratios of quantities measured on mirror points on the ordered/disordered sides of the transition, such as m_H/Δ and Υ/Δ, where Υ is the helicity modulus in the ordered phase (superfluid stiffness in the superfluid phase). For $N = 2$, we compute the high-frequency universal conductivity $\sigma_c^*(\omega \gg T)$ in the quantum-critical regime. In addition, we compute the universal ratio C/L between the low-frequency capacitance in the insulator and the inductance in the superfluid to one-loop order. These results are consistent with vortex-charge duality[12] relations between the two sides of the QCP.

Our results are relevant to recent experiments which probe critical dynamics. In cold-atomic gases, the Higgs mode has been excited by modulating the lattice potential near the superfluid to Mott transition.[7] Fast real-time pump-probe response was used to see amplitude oscillations in charge density wave (CDW) systems.[13,14] Raman and neutron scattering have long identified a *"two-magnon peak"* in antiferromagnets.[15–19]

Within our theory, this peak is a Higgs mode which would soften at criticality. The conductivity in cold-atom systems may be measured by lattice phase modulations.[20] For Josephson junction arrays and granular superconducting films, Coulomb interactions must be considered, as they give rise to massless two-dimensional plasmons. We show that this increases the power-law rise of the conductivity above the Higgs threshold. While our theory is for translationally invariant systems, some of the finite-frequency zero-wave-vector results may be a good starting point for understanding very recent results on disordered granular superconducting films.[21]

This paper is organized as follows. Section II presents the O(N) field theory and the observables we study, together with their expected scaling near the quantum-critical point. Section III introduces the discretized lattice model. In Sec. IV, we locate the critical point as a function of cutoff parameters and compute the relevant energy scales near the critical point. In Sec. V, we present the universal scaling functions of the scalar susceptibility. In Sec. VI, we compute the dynamical conductivity on both sides of the superfluid Mott transition and present an approximate duality for the optical conductivity. Appendix A describes the QMC algorithm in detail. Appendix B discusses the numerical analytical continuation procedure and provides an error analysis of the kernel pseudoinversion. Finally, Appendix C describes a weak coupling analytic calculation of the conductivity.

II. FIELD THEORY AND SCALING

We will study microscopic systems with O(N) symmetry whose long-wavelength and low-energy universal properties near the QCP are captured by a quartic field theory with relativistic dynamics.[4] The field theory in $(2 + 1)$-dimensional Euclidean space-time is given by

$$\mathcal{Z} = \int \mathcal{D}\vec{\phi}\, e^{-S[\vec{\phi}]},$$

$$S[\vec{\phi}] = \int_\Lambda d^2x\, d\tau \left[\frac{1}{2}(\partial_\mu \vec{\phi})^2 + \frac{1}{2}\mu \vec{\phi}^2 + g(\vec{\phi}^2)^2 \right]. \quad (1)$$

The fields $\vec{\phi}$ are N-component real fields, $\partial_\mu = \{\partial_\tau, \partial_x, \partial_y\}$, and Λ is an ultraviolet cutoff. Examples of physical realizations include the superfluid to Mott insulator transition of lattice bosons at commensurate fillings[1] for $N = 2$ and the Néel to singlet transition of dimerized Heisenberg antiferromagnets[2] for $N = 3$.

The system undergoes a quantum phase transition as the quantum tuning parameter g is varied. For $g < g_c$, the O(N) symmetry is spontaneously broken as the field obtains a nonzero expectation value $\langle \vec{\phi} \rangle \neq 0$. The ordered phase is then characterized by $N - 1$ massless Goldstone modes and a single gapped Higgs mode. For $g > g_c$, the system is disordered and contains N massive modes with excitation gap $\Delta(g)$. A dimensionless QCP tuning parameter is defined by $\delta g = (g - g_c)/g_c$.

We study two dynamical observables: the scalar susceptibility and the dynamical conductivity. For completeness, we define these observables and discuss their expected scaling behavior and experimental realizations.

A. Scalar susceptibility

The scalar susceptibility describes the response function of experimental probes that are sensitive to the amplitude of the order parameter, but not to its direction,[5] as discussed in the following. As an example, the scalar susceptibility has been recently measured in experiments on cold atoms on optical lattices near the Mott insulator superfluid transition.[7] The experimental protocol consists of modulating the optical lattice depth at a fixed frequency and measuring the energy absorbed using an *in situ* imaging technique.

The scalar susceptibility is defined as the correlation function of the order-parameter amplitude squared:

$$\chi_s(\tau) = \int d^2x \left(\langle \vec{\phi}^2_{x,y,\tau}\, \vec{\phi}^2_{\mathbf{0}} \rangle - \langle \vec{\phi}^2_{\mathbf{0}} \rangle^2 \right),$$

$$\chi_s(i\omega_m) = \int_0^\beta d\tau\, e^{i\omega_m \tau} \chi_s(\tau). \quad (2)$$

The real frequency spectral function is obtained by analytic continuation of Eq. (2):

$$\chi_s''(\omega) = -\mathrm{Im}\chi_s(i\omega_m \to \omega + i0^+). \quad (3)$$

Scaling arguments indicate that the expected low-energy form of Eq. (2) near the QCP is[8]

$$\chi_s(\omega/\Delta) \sim C + \mathcal{A}_\pm \Delta^{3-2/\nu} \Phi_\pm(\omega/\Delta), \quad (4)$$

where $\Delta \sim |\delta g|^\nu$ is the gap in the disordered phase, ν is the correlation-length critical exponent, and Φ_- (Φ_+) is a universal function of ω/Δ on the ordered (disordered) side of the transition. The nonuniversal constant C is real and is a regular function of g across the transition. The ordered phase is gapless due to the presence of Goldstone modes. In order to provide a well-defined energy scale that characterizes fluctuations on the ordered phase ($\delta g < 0$), we use the gap at the mirror point $-\delta g$ across the transition.

The scalar susceptibility captures the low-energy, universal response function of all experimental probes that couple to the order-parameter amplitude. To illustrate this point we consider, for example, experiments involving lattice amplitude modulations in the Bose-Hubbard model.[7] The response function in this case is given by the dynamical kinetic energy correlation function.[9] In order to relate this response function to the scalar susceptibility, we investigate the effective action near the quantum-critical point, written in terms of the order-parameter field $\Psi_B(x,\tau)$ (Ref. 4):

$$\mathcal{S}_B = \int d\tau\, d^2x \left[K_1 \left| \frac{\partial \Psi_B}{\partial \tau} \right|^2 + K_2 |\nabla \Psi_B|^2 \right.$$
$$\left. + r|\Psi_B|^2 + u|\Psi_B|^4 \right]. \quad (5)$$

The parameters K_1, K_2, r, u are all functions of the hopping amplitude t and the onsite interaction U. For instance, if the transition is tuned by varying the hopping amplitude t, then r can be linearized about the critical point as $r = r_0(t - t_c)$. Thus, the energy absorbed due to modulations of the hopping amplitude t can be described by the dynamical response of an operator of the form

$$\Theta(x,\tau) = \alpha|\Psi_B|^2 + \beta|\partial_t \Psi_B|^2 + \gamma|\nabla \Psi_B|^2 + \delta|\Psi_B|^4. \quad (6)$$

Close to the QCP, the term proportional to $|\Psi_B|^2$ will dominate the low-energy spectral weight since it is the most relevant operator in the long-wavelength limit. As a consequence, the universal part of the response function coincides with the scalar susceptibility.

B. Conductivity

The dynamical conductivity measures the response to an external gauge field. Our analysis will be restricted to the $N = 2$ case, as is relevant to dynamical conductivity measurements in superconductors and also to neutral cold atoms probed by optical lattice phase modulations.[20] To simplify the analysis, we write the two scalar fields in Eq. (1) as a single complex field $(\phi_1, \phi_2) = \sqrt{2}(\text{Re}\Psi, \text{Im}\Psi)$. We introduce the gauge field A_μ through minimal coupling $\partial_\mu \Psi \to (\partial_\mu + ie^* A_\mu)\Psi$ for a field Ψ carrying charge e^*.

The current is obtained by differentiating the action with respect to A_μ, viz.,

$$
\begin{aligned}
\langle J_\mu \rangle &= \frac{\delta S(A)}{\delta A_\mu} \\
&= ie^* \langle \Psi^* \partial_\mu \Psi - \Psi \partial_\mu \Psi^* \rangle + 2e^{*2} A_\mu \langle |\Psi|^2 \rangle,
\end{aligned} \quad (7)
$$

from which we derive the response function

$$
\begin{aligned}
\Pi_{\mu\nu}(x, x') &= \frac{\delta}{\delta A_\nu(x')} \langle J_\mu(x) \rangle \bigg|_{A=0} \\
&= \langle J_\mu(x) J_\nu(x') \rangle + 2e^{*2} \langle |\Psi|^2 \rangle \delta_{\mu\nu} \delta(x - x').
\end{aligned} \quad (8)
$$

The first term is the paramagnetic response kernel $\Pi_{\mu\nu}^{\text{P}}(x, x') = \langle J_\mu(x) J_\nu(x') \rangle$, and the second term is the diamagnetic response. The conductivity is then given by

$$
\sigma(i\omega_m) = -\frac{1}{\omega_m} \Pi_{xx}(i\omega_m, q = 0). \quad (9)
$$

As in Eq. (3), the real frequency dynamics is obtained by analytic continuation

$$
\sigma(\omega) = \sigma(i\omega_m \to \omega + i\epsilon). \quad (10)
$$

Remarkably, in $2 + 1$ dimensions the scaling dimension of the conductivity is zero.[22] As a result, near the critical point the conductivity has the scaling form[22,23]

$$
\sigma(\omega) = \sigma_Q \Sigma_\pm(\omega/\Delta). \quad (11)
$$

Here, $\sigma_Q = e^{*2}/h$ is the quantum of conductance and $\Sigma_\pm$ are dimensionless universal functions of ω/Δ for the disordered $(+)$ and ordered $(-)$ phases.

III. MODEL AND METHODS

In order to simulate the continuum field theory (1), we consider the following discrete lattice model:

$$
\begin{aligned}
\mathcal{Z} &= \int \mathcal{D}\vec{\phi} \, e^{-S[\vec{\phi}]}, \\
S &= \sum_{\langle ij \rangle} \vec{\phi}_i \cdot \vec{\phi}_j + \mu \sum_i |\vec{\phi}_i|^2 + g \sum_i |\vec{\phi}_i|^4.
\end{aligned} \quad (12)
$$

Here, $\vec{\phi}$ is an N-component scalar field, residing on the sites of cubic lattice of linear size L with periodic boundary conditions.

The model is the same as that considered in Ref. 10, as seen by rescaling $\vec{\phi}_i \to g^{-1/2}\vec{\phi}_i$. The long-wavelength properties of Eq. (12) are captured by the field theory (1). This model can be interpreted either as a quantum mechanical partition function in discrete $2 + 1$ Euclidean space-time dimensions or as a classical statistical mechanics model in three dimensions. Near the phase transition between ordered and disordered phases, this minimal model captures the critical properties of Eq. (1) while explicitly treating space and time on an equal footing and preserving exact particle-hole symmetry ($\Psi \to \Psi^*$) for the $N = 2$ case.

Next, we define the discrete lattice version of the continuum observables. The scalar susceptibility is given by

$$
\chi_s(\tau) = \sum_{x,y} \langle \vec{\phi}_{x,y,\tau}^2 \, \vec{\phi}_0^2 \rangle - \langle \vec{\phi}_0^2 \rangle^2. \quad (13)
$$

To define the conductivity, it is easier to consider the $U(1)$-symmetric complex field analog model of the $N = 2$ scalar field

$$
\begin{aligned}
\mathcal{Z} &= \int \mathcal{D}\Psi \, \mathcal{D}\Psi^* \, e^{-S[\Psi, \Psi^*]}, \\
S &= \sum_{\langle ij \rangle} \left(\Psi_i^* \Psi_j + \Psi_i \Psi_j^* \right) + 2\mu \sum_i |\Psi_i|^2 + 4g \sum_i |\Psi_i|^4.
\end{aligned} \quad (14)
$$

We introduce the gauge field $A_\mu(i)$ through Peierls substitution $\Psi_i^* \Psi_{i+\mu} \to \Psi_i^* \Psi_{i+\mu} e^{ie^* A_\mu(i)}$. The current is then

$$
J_\mu(i) = \frac{\delta S}{\delta A_\mu(i)} = ie^* \langle \Psi_i^* \Psi_{i+\hat{\mu}} e^{ie^* A_\mu(i)} - \text{c.c.} \rangle \quad (15)
$$

and the response function

$$
\begin{aligned}
\Pi_{\mu\nu}(i, j) &= \frac{\delta}{\delta A_\nu(j)} \langle J_\mu(i) \rangle \bigg|_{A=0} \\
&= \Pi_{\mu\nu}^{\text{P}}(i, j) + K \delta_{\mu\nu} \delta_{i,j}.
\end{aligned} \quad (16)
$$

$\Pi_{\mu\nu}^{\text{P}}(i, j) = \langle J_\mu(i) J_\nu(j) \rangle$ and $K = -e^{*2} \langle \Psi_i^* \Psi_{i+\hat{\mu}} + \text{c.c.} \rangle$ are the lattice versions of, respectively, the paramagnetic and the diamagnetic responses.

The simplicity of our model allowed us to simulate large system sizes, up to $L = 200$. Considering such large systems enabled us to accurately track the critical properties near the QCP. This is especially important in the ordered phase where the system is gapless and the dynamical response functions have power-law behavior. We implemented the highly efficient "worm algorithm"[24] sampling from a dual closed-loop representation. The correlation time of the worm algorithm scales well with system size, suppressing the critical slowing down near the transition. We also extend the work of Ref. 24 to treat general O(N) models with $N > 2$. Details of the QMC algorithm can be found in Appendix A. We compared our numerical results against previous QMC studies of O(N) models[25,26] and with analytically solved limits and found good agreement within error bars.

A key ingredient of our analysis is the numerical analytic continuation of imaginary-time QMC data to real frequency spectral functions. To do so, we have to invert the relation

$$
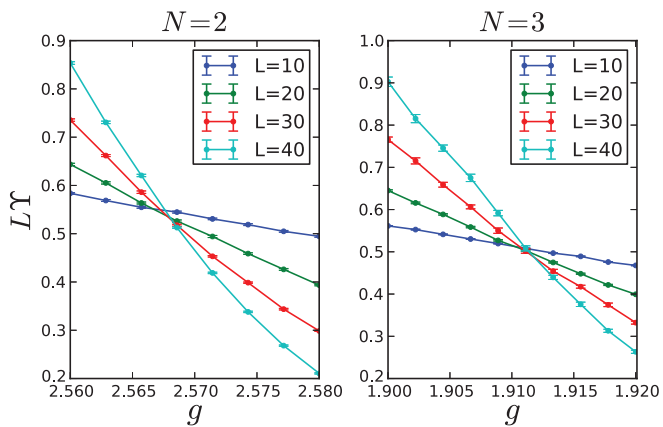\mathcal{G}(i\omega_m) = \int_0^\infty \frac{d\nu}{\pi} \frac{2\nu}{\omega_m^2 + \nu^2} A(\nu). \quad (17)
$$

FIG. 1. (Color online) Curves of $L\Upsilon$ for a sequence of increasing system size L for O($N = 2, 3$) models. The curves cross at a single point, from which we determine the value of g_c. Here, we take $\mu = -0.5$ and $g_c = 2.568(2)$ for the $N = 2$ case and $g_c = 1.912(2)$ for $N = 3$.

Here, $\mathcal{G}(i\omega_m)$ is a correlation function in Matsubara frequency space, evaluated by the QMC simulation, and $A(\nu)$ is the spectral function. However, the kernel has very small singular value eigenvalues, and the inversion can unwittingly amplify the statistical QMC noise in $\mathcal{G}(i\omega_m)$. A detailed discussion of methods which can circumvent these artifacts is presented in Appendix B.

IV. CRITICAL ENERGY SCALES

A. Determination of the critical coupling

In order to study critical properties, it is necessary to locate the QCP with high accuracy. We determine the critical coupling by finite-size scaling analysis of the helicity modulus of the $(2 + 1)$-dimensional quantum model. The helicity modulus Υ is defined by $\Upsilon \equiv \frac{1}{L} \frac{\partial^2 \ln \mathcal{Z}(\varphi)}{\partial \varphi^2}|_{\varphi=0}$ where $\mathcal{Z}(\varphi)$ is the partition function in the presence of a uniform phase twist φ. Near the critical point, ΥL is a universal constant, with only next-to-leading-order corrections in the system size L.[22,27] The critical coupling is then determined from the crossing point of $L\Upsilon$ for a sequence of increasing system sizes L. Illustrative examples for $N = 2$ and 3 are shown in Fig. 1. Curves for different system sizes cross at a single point with little variation with system size, allowing us to determine the critical coupling accurately.

We studied a few different parameter sets (g_c, μ_c) which are shown in Table I. The use of multiple sets of model parameters for $N = 2$ allowed us to test the universality of our results. In

TABLE I. List of model parameters studied, along with their critical couplings.

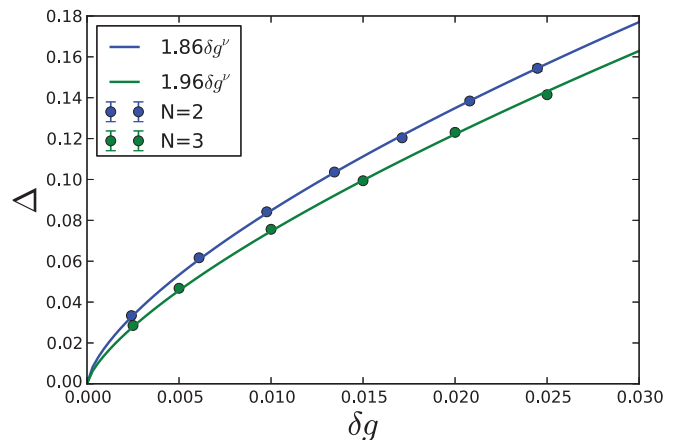| Model	N	Model parameters	Critical coupling
A	2	$\mu = -0.5$	$g_c = 2.568(2)$
B	2	$\mu = -2$	$g_c = 3.908(2)$
C	2	$g = 7.6923$	$\mu_c = -5.883(2)$
D	3	$\mu = -0.5$	$g_c = 1.912(2)$
E	4	$\mu = -0.5$	$g_c = 1.516(2)$

FIG. 2. (Color online) Scaling of the gap $\Delta(\delta g)$ in the disordered phase for $N = 2, 3$ and $\mu = -0.5$. Fitting to the scaling form $\Delta = \Delta_0(\delta g)^\nu$ gives $\Delta_0 = 1.86(1)$ for $N = 2$, $\mu = -0.5$, and $\Delta_0 = 1.96(1)$ for $N = 3$, $\mu = -0.5$. Error bars are smaller than the symbols.

most cases, we tuned the transition by varying g, except in the case of dynamical conductivity, where we varied μ.

B. Excitation gap in the disordered phase

The gap in the disordered phase provides a reference energy scale for all dynamical properties. It can be extracted with high precision from the zero-momentum two-point Green's function[28]

$$G(\tau) = \sum_{x,y} \langle \vec{\phi}_{x,y,\tau} \cdot \vec{\phi_0} \rangle, \qquad (18)$$

without recourse to analytic continuation. At large imaginary times, $G(\tau)$ is expected to behave as

$$G(\tau) \sim e^{-\Delta\tau} + e^{-\Delta(\beta-\tau)}. \qquad (19)$$

The gap Δ is evaluated by a fit to the above functional form. The evolution of the gap near the QCP is depicted in Fig. 2 for $N = 2, 3$. The gap softens as $\delta g \to 0$ according to the scaling form $\Delta(g) \sim \Delta_0(\delta g)^\nu$, from which we extract Δ_0. For the correlation-length exponent ν, we use values determined in previous high-accuracy simulations[25,26]: $\nu_2 = 0.6723(3)$, $\nu_3 = 0.710(2)$, and $\nu_4 = 0.749(2)$ for $N = 2, 3$, and 4, respectively.

We validated our results by performing a similar analysis of the long imaginary-time form of the scalar susceptibility[10] $\chi_s(\tau) \sim \tau^{-1} e^{-2\tau\Delta}$. We found good agreement between the two approaches.

C. Helicity modulus in the ordered phase

In two spatial dimensions, the helicity modulus is an energy scale that can be used to characterize the ordered phase. For $N = 2$ ($N = 3$) it plays the role of the superfluid stiffness (spin stiffness). Similarly to the gap in the disordered phase, the helicity modulus near the QCP vanishes according to the scaling behavior $\Upsilon = \Upsilon_0(\delta g)^\nu$ (see Fig. 3). The ratio Υ_0/Δ_0 is universal. We find $\Upsilon_0/\Delta_0 = 0.44(1)$ for $N = 2$ and $\Upsilon_0/\Delta_0 = 0.34(1)$ for $N = 3$. This universal ratio was also calculated by means of nonperturbative renormalization group methods in Ref. 29.
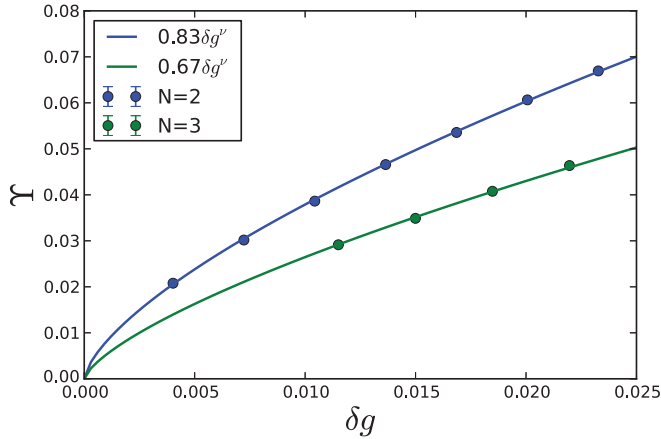
FIG. 3. (Color online) Scaling of the helicity modulus $\Upsilon(\delta g)$ in the ordered phase for $N = 2,3$ and $\mu = -0.5$. Fitting to the scaling form $\Upsilon = \Upsilon_0(\delta g)^\nu$ gives $\Upsilon_0 = 0.83(1)$ for $N = 2$, $\mu = -0.5$ and $\Upsilon_0 = 0.67(1)$ for $N = 3$, $\mu = -0.5$. Error bars are smaller than the symbols.

V. SCALAR SUSCEPTIBILITY

In the following, the universal scaling functions of the scalar susceptibility are computed for both phases.

A. Matsubara frequency universal scaling function

In Fig. 4(a), numerical results for the $N = 2$ scalar susceptibility $\chi_s(i\omega_m)$ as a function of Matsubara frequency are presented for both phases. The scaling form (4) applies also to the correlation function in Matsubara space. The universal scaling function $\Phi(i\omega_m)$ is then computed by rescaling the $\chi_s(i\omega_m)$ curves according to Eq. (4). The collapse requires the extraction of the nonuniversal real constant C, which is expected to be a smooth function of δg. We find C by fitting $\chi_s(i\omega_m)$ at small ω_m to a polynomial in δg, and then subtracting

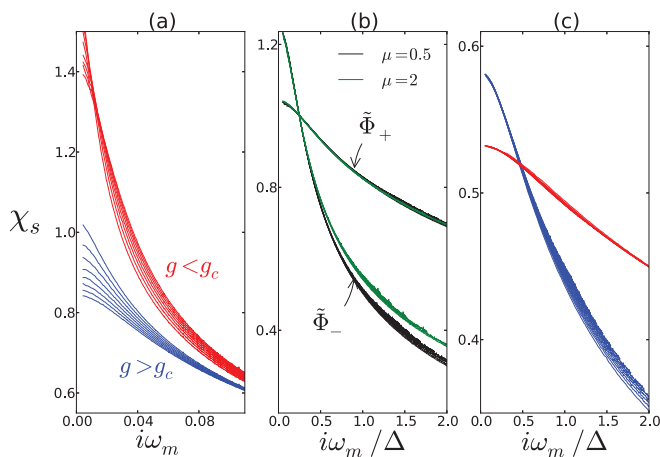

FIG. 4. (Color online) (a) The scalar susceptibility $\chi_s(i\omega_m)$ for $N = 2$. The curves correspond to different values of δg below and above the phase transition. (b), (c) Universal scaling function after rescaling for $N = 2,3$. In (b) we show the scaling function for two crossing points of the phase transition. The two rescaled curves agree very well, especially at low frequencies. Simulations were performed with $\mu = 0.5$ and 2 for $N = 2$ and $\mu = 0.5$ for $N = 3$.
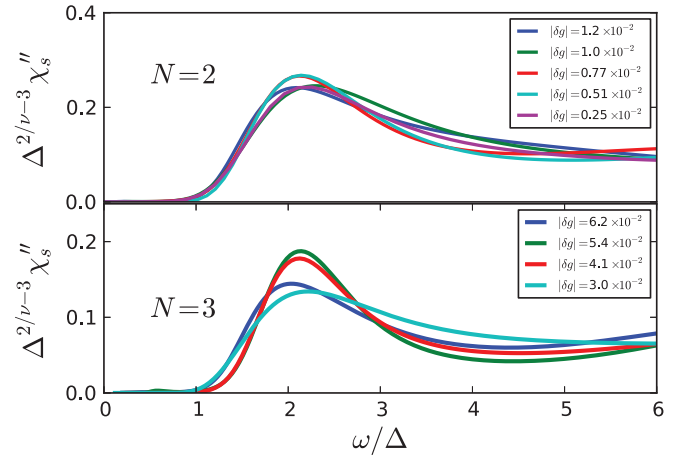

FIG. 5. (Color online) $\chi_s''(\omega)$ in the ordered phase for $N = 2$ and 3. We scale the curves according to Eq. (4) for a range of tuning parameters δg near the critical point.

it from $\chi_s(i\omega_m)$. The ω axis is then rescaled by Δ and the vertical axis is rescaled by $\Delta^{3-2/\nu}$.

Figures 4(b) and 4(c) show the scaling procedure for $N = 2,3$. The curves collapse into two universal functions $\Phi_\pm(i\omega_m)$. To test the universality of our results, we repeated the scaling analysis at a different crossing point of the phase transition for the $N = 2$ case. The results are presented in Fig. 4(b). The scaled curves for both sets of critical couplings agree very well, especially for low frequencies. This provides a stringent test for the consistency of our analysis.

B. Real frequency universal scaling function

Next, we examine the imaginary part of the retarded response function $\chi_s''(\omega)$ obtained from analytic continuation of $\chi_s(i\omega_m)$. To extract the universal part of the line shape we rescale the ω axis by Δ and the vertical axis by $\Delta^{3-2/\nu}$. Note that this rescaling is done without any free-fitting parameters since the real constant C in Eq. (4) drops out from the spectral function.

The rescaled line shape in the ordered phase is shown in Fig. 5 for $N = 2$ and 3. Curves for different values of δg collapse into a single universal line shape especially at low frequencies. The line shape contains a clear peak that can be associated with the Higgs mode. Our analysis demonstrates that the Higgs peak is a universal feature in the spectral function that survives as a resonance arbitrarily close to the critical point.

Some universal values can be obtained by this analysis. For example, we consider the ratio between the Higgs mass in the ordered phase, defined by the maximum in $\chi_s''(\omega)$, and the gap in the disordered phase at mirror points across the transition. This ratio is found to be $m_H/\Delta = 2.1(3)$ and $m_H/\Delta = 2.2(3)$ for $N = 2$ and 3, respectively. We also obtain the fidelity $F = m_H/\Gamma$, where Γ is the full width at half-maximum. We measure Γ with respect to the leading edge at low frequency since at low frequencies there is less contamination from the high-frequency nonuniversal spectral weight. Since the entire functional form of the line shape is universal, F is a universal
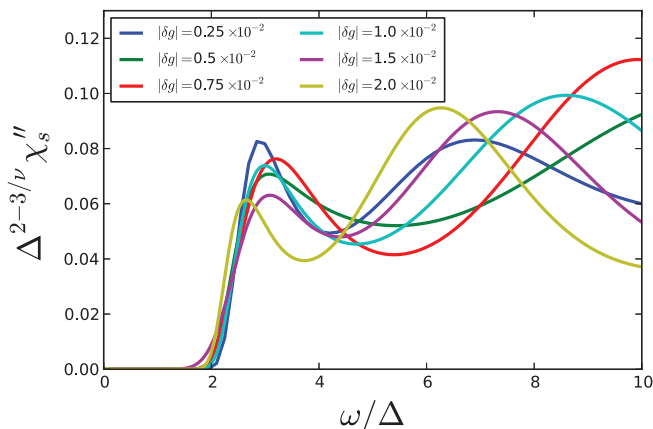
FIG. 6. (Color online) $\chi_s''(\omega)$ in the disordered phase for $N = 2$. We scale the curves according to Eq. (4) for a range of tuning parameters δg near the critical point.

constant that characterizes the shape of the peak. We find $F = 2.4(10)$ for $N = 2$ and $F = 2.2(10)$ for $N = 3$.

The rescaled spectral function in Fig. 5 shows higher variability at high frequencies than at low frequencies. We attribute this to contamination from the nonuniversal part of the spectrum and to systematic errors introduced by the maximum entropy ("MaxEnt") regularization of the analytic continuation, which is noisy in this regime.

In Fig. 6, we plot the rescaled line shape in the disordered phase for $N = 2$. The universal spectral function is gapped for $\omega < 2\Delta$ and rises sharply above the threshold. This behavior is in accordance with analytic predictions[8] and with previous QMC numerical simulation.[11] Previous studies found a Higgs-type resonance in the disordered phase above the threshold.[9,11] However, we find that the peak seen in Fig. 6 at $\omega/\Delta \approx 3$ is very shallow relative to the background spectral weight. Thus, we do not consider this to be conclusive evidence of a resonance. We note that numerical analytic continuation tends to produce oscillatory behavior near sharp features of the spectral function[30] and hence it is possible that the shallow peak might be an artifact of such an effect. For comparison, in Fig. 7 we show representative curves for the line shape on mirror points of the transition. If a resonance is at all present in the disordered phase, it is much less pronounced than in the ordered phase.

1. Asymptotic power-law decay of the scalar susceptibility

In the ordered phase, the low-frequency rise of the scalar susceptibility was predicted[5,8,31] to be

$$\Phi_-''(\omega) \sim (\omega/\Delta)^3, \quad \omega \ll \Delta \ll 1. \quad (20)$$

The ω^3 rise is due to the decay of a Higgs mode into a pair of Goldstone modes. Equation (20) transforms into the large imaginary-time asymptotic form $\chi_s(\tau) \sim 1/\tau^4$. Hence, to test Eq. (20) we examine the large-τ behavior of $\chi_s(\tau)$. We note that this approach does not rely on analytic continuation, enabling us to study the low-frequency dynamics in a numerically stable and well-controlled manner.

In Fig. 8, we present $\chi_s(\tau)$ on a log-log plot for $N = 3,4$ in the disordered phase with the detuning parameter $\delta g = 0.1 \times 10^{-2}$. For $N = 3,4$ we indeed find agreement with the
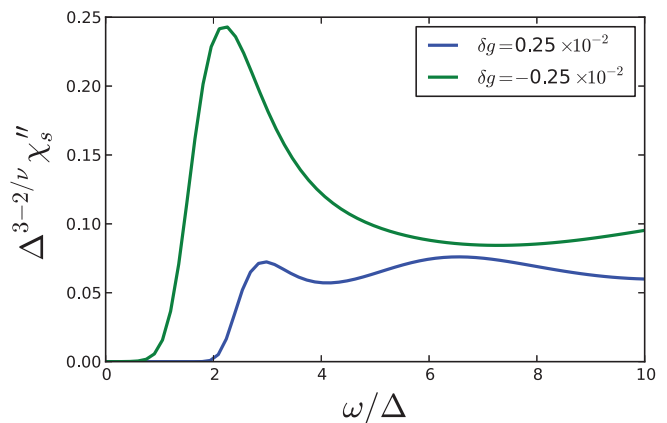

FIG. 7. (Color online) Comparison of the scalar susceptibility line shape $\chi_s''(\omega)$ on mirror points across the phase transition for $N = 2$. The blue green curve corresponds to disordered phase and the green curve to the ordered phase.

asymptotic behavior $\chi_s(\tau) \sim 1/\tau^4$ within the error bars. In Fig. 9, we present $\chi_s(\tau)$ for $N = 2$ on a log-log plot and on a semilog plot. Interestingly, for $N = 2$ we do not find a conclusive asymptotic falloff as $1/\tau^4$. Instead, the data fit better to an exponential decay, as in the disordered phase. This indicates that the ω^3 subgap spectral weight, if at all present, is small compared to the spectral weight contained in the Higgs peak. Indeed, we find excellent agreement between the large-τ exponential decay rate and the value of m_H obtained from the MaxEnt analysis, further supporting our results for the Higgs mass. We note that a $1/\tau^4$ power-law behavior might be regained at larger values of τ, but this lies below the statistical inference of our data.

Accurate determination of the scalar susceptibility at zero Matsubara frequency $\chi_s(i\omega = 0)$ is crucial for this analysis. Errors in $\chi_s(i\omega = 0)$ translate into an overall vertical shift of $\chi_s(\tau)$. This error can dominate the value of $\chi_s(\tau)$, especially at large τ where $\chi_s(\tau)$ is numerically small, and can lead to a bias in the power-law analysis. Typically, $\chi_s(i\omega = 0)$ is measured from a fluctuation relation $\chi_s(i\omega = 0) = \sum_{x,y,\tau} \langle \vec{\phi}_{x,y,\tau}^2 \vec{\phi}_0^2 \rangle - \langle \vec{\phi}_0^2 \rangle^2$ and hence does not self-average[32] upon increasing
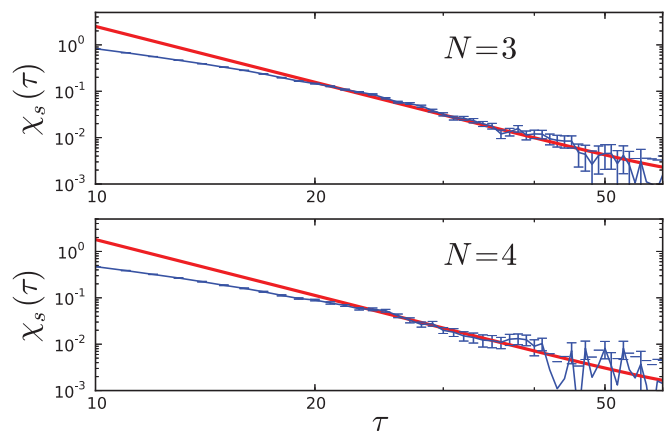

FIG. 8. (Color online) Log-log scale plot for $\chi_s(\tau)$ in the ordered phase. For $N = 3,4$, we indeed find the asymptotic behavior $\chi_s(\tau) \sim 1/\tau^4$ to agree within the error bars.
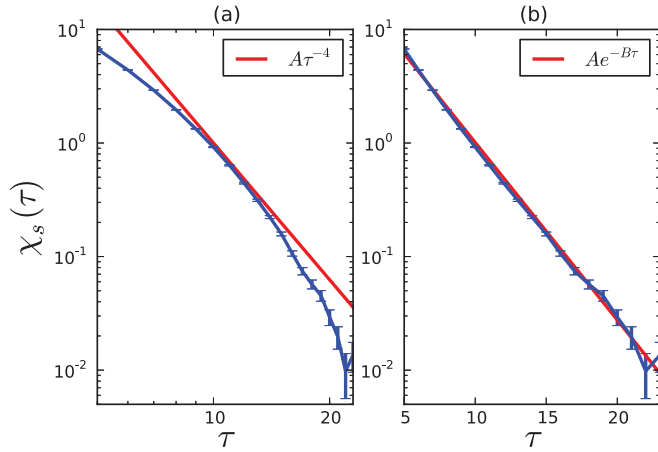
FIG. 9. (Color online) $\chi_s(\tau)$ in the ordered phase for $N = 2$, plotted on a log-log scale in panel (a) and a semilog scale in panel (b). The curve deviates significantly from the expected $1/\tau^4$ power-law form. Instead, the curve fits better to an exponential decay as in the disordered phase.

the system size. To overcome this difficulty, we computed $\chi_s(i\omega = 0)$ using a direct numerical derivative $\chi_s(i\omega = 0) = -d\langle \vec{\phi}^2 \rangle/d\mu$. To do so, we evaluated $\langle \phi^2 \rangle$ for a set of values of μ within a narrow range $[\mu - \Delta\mu, \mu + \Delta\mu]$ and extracted the derivative by a polynomial fit in μ. We found that this method reduced the error in $\chi_s(i\omega = 0)$ by an order of magnitude and significantly improved the power-law decay analysis.

VI. DYNAMICAL CONDUCTIVITY

In Fig. 10, we present the dynamical conductivity in the disordered and ordered phases. In both cases, the frequency axis ω is rescaled by Δ, noting that there is no need for a vertical rescaling since the conductivity is a universal amplitude. In both phases, the curves collapse into a single universal shape, especially at low frequencies. The spectrum on the disordered side has a clear gaplike behavior up to a threshold frequency
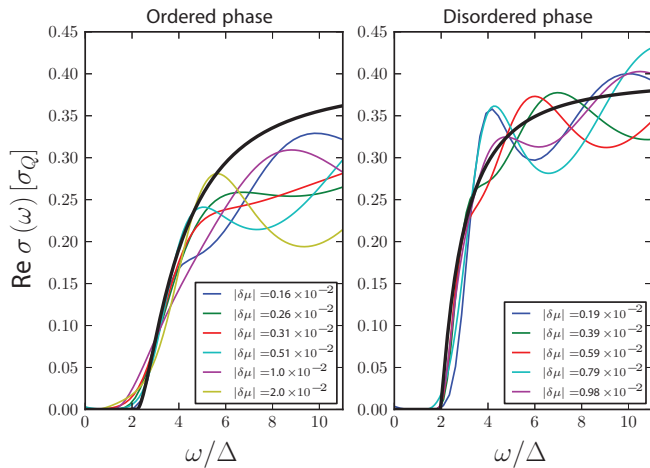

FIG. 10. (Color online) The optical conductivity $\mathrm{Re}\,\sigma(\omega)$ in the ordered and disordered phases for $N = 2$. Curves are scaled according to Eq. (11) for several values of the quantum tuning parameter δg near the critical point. The solid black curves show the analytic results from Refs. 5 and 23.

2Δ. Beyond this threshold, the spectrum rises sharply and saturates at a universal value of $\sigma_{\mathrm{dis}}(\omega \gg \Delta) \approx 0.35(5)\,\sigma_Q$, where $\sigma_Q = e^{*2}/h$ is the quantum of conductance. These results should be compared with the line shape calculated diagrammatically in Ref. 23:

$$\sigma_+(\omega) = 2\pi\sigma_Q \left(\frac{\omega^2 - 4\Delta^2}{16\omega^2} \right) \Theta(\omega - 2\Delta). \qquad (21)$$

Similarly, in the ordered phase, the dynamical conductivity grows rapidly starting at a threshold frequency $\approx 2\Delta$, and saturates at high frequency at a value $\sigma_{\mathrm{ord}}(\omega \gg \Delta) \approx 0.25(5)\,\sigma_Q$. A calculation to leading order in weak coupling predicts[5,6] (see also Appendix C)

$$\sigma_-(\omega) = 2\pi\sigma_Q \left(\frac{\omega^2 - m_H^2}{4\omega^2} \right)^2 \Theta(\omega - m_H). \qquad (22)$$

In contrast to the disordered phase, there is a subgap component to the conductivity, owing to the gaplessness of the Goldstone mode(s). This feature is first evident at two-loop order in a perturbative calculation of the conductivity. This was computed in Ref. 5, where it was found that the corresponding subthreshold ($\omega < m_H$) contribution to $\sigma(\omega)$ is

$$\sigma_-(\omega)|_{\omega < m_H} = \sigma_Q \frac{g m_H}{2^8 \pi} \left\{ \frac{N-2}{N} \left(\frac{16\omega}{15 m_H} + \frac{32\omega^3}{105 m_H^3} \right) \right.$$
$$\left. + \frac{3N-5}{N} \frac{16\omega^5}{315 m_H^5} + \cdots \right\} + \mathcal{O}(g^2). \quad (23)$$

Remarkably, for $N = 2$, the two leading-order frequency terms in the subthreshold conductivity vanish, resulting in a pronounced pseudogap behavior. Our numerical results appear to be qualitatively consistent with this analytic prediction. However, the coefficient of the leading ω^5 term is small, given by $3.2 \times 10^{-5}\,g/m_H^4$, and is not resolved within our numerical accuracy.

For comparison, the analytic curves corresponding to Eqs. (21) and (22) are plotted in Fig. 10. The value of m_H was taken from the scalar susceptibility analysis[10] and Δ from the gap analysis. There is a remarkable agreement between analytic and numerical curves especially at low frequencies. It is important to notice that analytic curves are presented without any fitting parameters (after setting m_H and Δ).

On general grounds, one expects the high-frequency ($\omega \gg \Delta$) limit of the universal conductivity functions to be equal on both ordered and disordered phases. Here, we find slightly different values $\sigma_{\mathrm{dis}}(\omega \gg \Delta) \approx 0.35(5)\,\sigma_Q$ and $\sigma_{\mathrm{ord}}(\omega \gg \Delta) \approx 0.25(5)\,\sigma_Q$, although there is significant spread which we attribute to limitations of the analytic continuation. This high-frequency value should also match the universal conductivity in the quantum-critical regime at high frequencies ($\Delta = 0$ and $\omega \gg T$). Taking an average over both results, we estimate $\sigma_c^*(\omega \gg T) \approx 0.3(1)\,\sigma_Q$. This value should be compared with the value $\sigma_c^* = 0.39\,\sigma_Q$ obtained in the large-N limit in Ref. 23, and with $\sigma_c^* = 0.251$ (Ref. 33) obtained from the leading correction in $1/N$. In addition, previous QMC simulations found $\sigma_c^* = 0.33\,\sigma_Q$ (Ref. 27) and $\sigma_c^* = 0.285\sigma_Q$ (Ref. 33).

A. Charge-vortex duality of the dynamical conductivity

The model in Eq. (1) with $N = 2$ describes relativistic bosons in $2 + 1$ dimensions. This system has a dual representation in terms of vortices.[12] Interestingly, the conductivity of the bosons is inversely proportional to the conductivity of the vortices,[33] such that

$$\sigma_{\text{B}}(\omega) = \frac{\sigma_{\text{Q}}^2}{\sigma_{\text{V}}(\omega)}. \tag{24}$$

Here, $\sigma_{\text{B}} = \sigma$ is the physical conductivity of the bosons, and σ_{V} is the vortex conductivity in response to a dual electric field, that is, a current of bosons. This relation is a direct consequence of the duality transformation and is therefore exact.

In the dual picture, the vortices interact with an inverse coupling constant. This fact can be used to relate physical properties on opposite sides of the transition. This mapping is not exact due to the different interaction laws of bosons and vortices: the bosons have contact interactions whereas the vortices have long-ranged interactions. This discrepancy prevents us from deriving exact results from the duality relation, yet it can be used to construct approximate or qualitative results. This relation was used in previous studies to estimate the dc conductivity at the critical point where the vortices and bosons are self-dual, hence, $\sigma_{\text{B}} = \sigma_{\text{V}} = \sigma_{\text{Q}}$. This simple argument, although not exact, gives the correct order of magnitude for the dc conductivity at the QCP.

Here, we ask whether this approach can be extended to the dynamical conductivity. Duality maps the conductance of symmetric points on both sides of the transition:

$$\sigma_{\text{B}}(\omega, -\delta g) = \sigma_{\text{V}}(\omega, \delta g). \tag{25}$$

This relation, combined with Eq. (24), yields a relation between the optical conductivities on both sides of the transition:

$$\sigma_{\text{B}}(\omega, -\delta g) = \frac{\sigma_{\text{Q}}^2}{\sigma_{\text{B}}(\omega, \delta g)}. \tag{26}$$

Here, $\sigma_{\text{B}}(\omega, \delta g)$ is complex, containing both dissipative and reactive parts $\sigma_{\text{B}} = \sigma_{\text{B}}' + i\sigma_{\text{B}}''$, such that

$$\sigma_{\text{B}}'(\omega, -\delta g) = \frac{\sigma_{\text{Q}}^2 \, \sigma_{\text{B}}'(\omega, \delta g)}{\sigma_{\text{B}}'^2(\omega, \delta g) + \sigma_{\text{B}}''^2(\omega, \delta g)}, \tag{27}$$

$$\sigma_{\text{B}}''(\omega, -\delta g) = -\frac{\sigma_{\text{Q}}^2 \, \sigma_{\text{B}}''(\omega, \delta g)}{\sigma_{\text{B}}'^2(\omega, \delta g) + \sigma_{\text{B}}''^2(\omega, \delta g)}. \tag{28}$$

Note that duality flips the sign of the reactive component.

Numerically we found it difficult to extract the reactive part of the conductivity. The results for the analytic continuation were much less numerically stable than for the dissipative component. Yet, the numerics do provide some evidence for the duality. According to Eq. (27), one prediction of duality is that whenever the dissipative part vanishes for some frequency ω in one of the phases, it must also vanish at the mirror point in the other phase. This is indeed seen to be the case in Fig. 10, where the threshold frequency of the dissipative part of the optical conductivity equals $\omega_{\text{T}} \sim 2\Delta$ on *both* sides of the transition. The presence of small subgap conductivity in the superfluid is a consequence of the inexactness of the duality.

As an additional test of the duality, in Appendix C we present analytic calculations of the optical conductivity on both
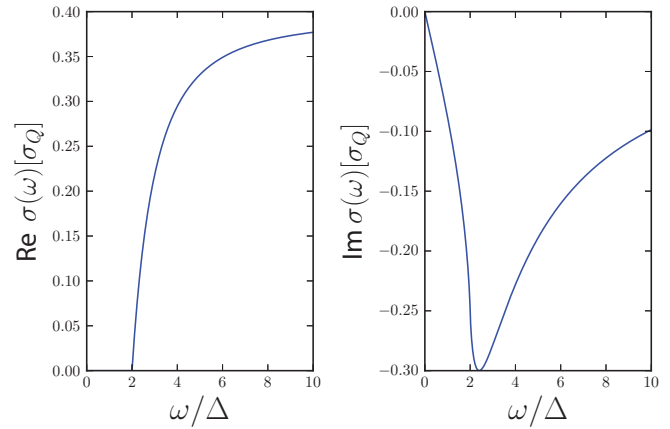

FIG. 11. (Color online) The real and imaginary parts of the optical conductivity in the disordered phase. Results are shown from a one-loop calculation in Appendix C.

sides of the transition, to one-loop order. In Figs. 11 and 12, we show the dynamical conductivity on the ordered and disordered phases, respectively. In order to use the same reference energy scale in both figures, we used the universal values $m_H/\Delta = 2.1$ and $\rho_s/\Delta = 0.44$ obtained numerically in earlier parts of the analysis. In Fig. 12, we also depict the conductivity in the ordered phase, as obtained by applying the duality [Eq. (26)] to the conductivity in the disordered phase. As in the dc case, the overall scale of the conductivity has the right order of magnitude, set by σ_{Q}, but is not quantitative. However, the functional form of the conductivity is well captured by the duality.

Interestingly, duality makes a strong prediction on the reactive component of the conductivity at low frequencies. A superfluid acts as a perfect inductor at low frequencies, with admittance $\sigma_{\text{B}}''(\omega) = 1/\omega L_{\text{ord}}$, where the inductance is $L_{\text{ord}} = \hbar/(2\pi\sigma_{\text{Q}}\rho_s)$.[34] According to Eq. (28), using the fact that the dissipative part is negligible for $\omega \ll \Delta$, this implies that at low frequencies the disordered phase behaves as a capacitor,
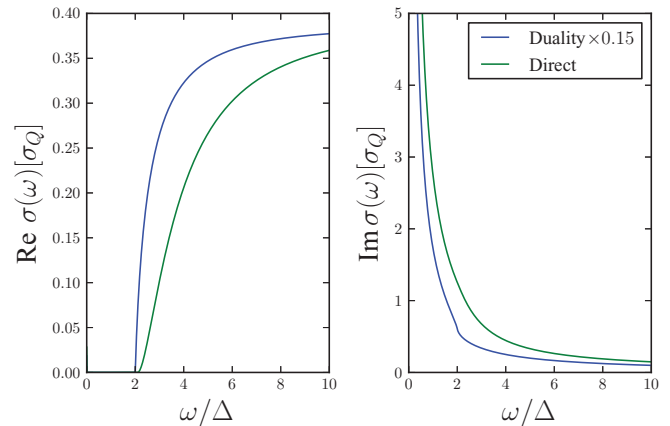

FIG. 12. (Color online) The real and imaginary parts of the optical conductivity in the ordered phase. The green curve displays the results of a one-loop calculation carried in Appendix C. The values of m_H/Δ and ρ_s/Δ were taken from the QMC simulation. The blue curve depicts the optical conductivity obtained from the duality relation in Eq. (26). This curve is multiplied by 0.15 for comparison reasons.

with admittance is $\sigma_B''(\omega) = -\omega C_{\mathrm{dis}}$, where the capacitance is $C_{\mathrm{dis}} = \sigma_Q \hbar/(2\pi\rho_s)$. Physically, this capacitance measures the polarizability of the bosons in the presence of an external electric field. Furthermore, if the duality were exact, the universal ratio between the capacitance in the disordered phase and the inductance in the ordered phase would be $C_{\mathrm{dis}}/L_{\mathrm{ord}} = \sigma_Q^2$. Indeed, we find that at low frequencies the optical conductivity in the disordered phase, computed in Appendix C, rises linearly as $\sigma_{\mathrm{dis}}''(\omega) = -2\pi\sigma_Q \times \hbar\omega/(24\pi\Delta) + \mathcal{O}(\omega^2)$, that is, as a capacitor with capacitance $C_{\mathrm{dis}} = 2\pi\sigma_Q \times \hbar/(24\pi\Delta)$. This yields the ratio

$$\frac{C_{\mathrm{dis}}}{L_{\mathrm{ord}}} = \frac{2\pi\rho_s}{12\Delta}\sigma_Q^2 \approx 0.23\,\sigma_Q^2, \tag{29}$$

where in the last equality we used $\rho_s/\Delta = 0.44$ as obtained in Sec. IV C.

An illuminating way to understand the low-frequency conductivity is through the dual-vortex representation. In this representation, the effective field theory is given by a complex ψ^4 theory coupled to an electromagnetic gauge field:[35,36]

$$\mathcal{S} = \int d^3x \left\{ |(\partial_\mu + ia_\mu)\psi|^2 + m^2|\psi|^2 + \lambda|\psi|^4 \right.$$
$$\left. + \frac{1}{16\pi^2 K}\,f_{\mu\nu}f_{\mu\nu} \right\}. \tag{30}$$

Here, the complex field ψ is the vortex condensate order-parameter field, $f_{\mu\nu} = \partial_\mu a_\nu - \partial_\nu a_\mu$, and K is the coupling constant of the bosons. The gauge field a_μ is related to the original boson 3-current by

$$J_\mu = \frac{1}{2\pi}\,\epsilon_{\mu\nu\lambda}\partial_\nu a_\lambda. \tag{31}$$

Since the current is equal to the dual electric field $J_x(i\omega_m) = -\omega_m a_y/2\pi$, the conductivity is

$$\sigma(i\omega_m) = -\frac{1}{\omega_m}\langle J_x(i\omega_m)\,J_x(-i\omega_m)\rangle$$
$$= \frac{\omega_m}{(2\pi)^2}\langle a_y(i\omega_m)\,a_y(-i\omega_m)\rangle. \tag{32}$$

In the disordered vortex phase, corresponding to the superfluid phase of the original bosons, the gauge field remains gapless with the propagator in the Feynman gauge:

$$\langle a_\mu\,a_\nu \rangle = \frac{4\pi^2 K}{k^2}\,\delta_{\mu\nu}, \tag{33}$$

hence, the conductivity is $\sigma_{\mathrm{ord}}(i\omega_m) = K/\omega_m$. After analytic continuation and introducing physical units $e^{*2}/\hbar = 2\pi\sigma_Q$, this becomes

$$\sigma_{\mathrm{ord}}(\omega) = 2\pi\sigma_Q \frac{\rho_s}{\hbar}\left[\frac{i}{\omega} + \pi\delta(\omega)\right], \tag{34}$$

where we have set $K = \rho_s$, its value in the superfluid phase. In the condensed vortex state, corresponding to the disordered phase of the original bosons, the field ψ gets an expectation value leading to a mass term for the gauge field through the Anderson-Higgs mechanism. The effective action of the gauge field is then given by a Proca action:

$$\mathcal{S} = \int d^3x \left\{ \frac{1}{16\pi^2 K}\,f_{\mu\nu}f_{\mu\nu} + \frac{1}{2}\rho_v a_\mu^2 \right\}, \tag{35}$$

where we now take the vortex condensation density $\rho_v = 2|\langle\psi\rangle|^2$. The gauge field propagator is

$$\langle a_\mu\,a_\nu \rangle = \frac{4\pi^2 K}{k^2 + M^2}\left(\delta_{\mu\nu} - \frac{k_\mu k_\nu}{M^2}\right), \tag{36}$$

where the gauge field mass M is given by $M^2 = 4\pi^2 K\rho_v$. Note that since the current is quadratic in boson operators, this mass is related to the single-boson gap Δ by $M = 2\Delta$. Now, the conductivity is given by $\sigma_{\mathrm{dis}}(i\omega_m) = \omega_m K/(\omega_m^2 + M^2)$, which yields after analytic continuation $\sigma_{\mathrm{dis}}(\omega) = i\omega K/(\omega^2 - M^2)$. At low frequencies $\omega \ll M$ this becomes, in physical units,

$$\sigma_{\mathrm{dis}}(\omega) \approx -2\pi i\sigma_Q \frac{K}{M^2}\hbar\omega = -i\sigma_Q \frac{\hbar\omega}{2\pi\rho_v}. \tag{37}$$

Combining the results from Eqs. (34) and (37), we obtain

$$\frac{C_{\mathrm{dis}}}{L_{\mathrm{ord}}} = \frac{\rho_s}{\rho_v}\sigma_Q^2. \tag{38}$$

This gives a physical interpretation for the universal ratio C/L as the ratio between the superfluid stiffness and the vortex condensation density on opposite sides of the transition.

B. Effect of Coulomb interactions

Josephson junction arrays and granular superconducting films can often be described by charged lattice bosons,[37] which interact at long range via e^2/r Coulomb interactions. When Coulomb interactions are present, the O(N) model Lagrangian should be augmented by a contribution

$$\Delta L = \int d^2x\,in\frac{\partial\varphi}{\partial\tau} + \frac{1}{2}\int d^2x \int d^2x'\,n(\boldsymbol{x})\frac{e^{*2}}{|\boldsymbol{x}-\boldsymbol{x}'|}\,n(\boldsymbol{x}'), \tag{39}$$

where φ is the phase of the order parameter. We parametrize the $\vec{\phi}$ field in terms of longitudinal (σ) and transverse (π) fluctuations:

$$\vec{\phi} = (\phi_0 + \sigma\,,\,\pi), \tag{40}$$

where $\phi_0 \equiv |\langle\vec{\phi}\rangle|$. To lowest order, we have $\varphi = \pi/\eta\sqrt{N}$, where $\eta \equiv \phi_0/\sqrt{N}$ is proportional to the magnitude of the order parameter. Integrating out the density field $n(\boldsymbol{x},\tau)$, we find that the π propagator becomes

$$G_{\pi\pi}(q) = \frac{1}{q_0^2 + \boldsymbol{q}^2 + \alpha\,|\boldsymbol{q}|\,q_0^2}, \tag{41}$$

where $\alpha = \eta g\hbar v/\pi e^{*2}$ and v is the velocity ("speed of light") in the original O(N) model. This new π-field propagator has a two-dimensional (2D) plasmon pole located at $q_0 = \sqrt{-|\boldsymbol{q}|/\alpha}$ for small $\boldsymbol{q}$. Plugging this into the expression for the electromagnetic kernel, in Eq. (E1) of Ref. 5, we find, to order g^0,

$$\sigma(\omega) = 2\sigma_Q \left(\frac{\alpha}{m_H}\right)^2 (\omega - m_H)^4\,\Theta(\omega - m_H). \tag{42}$$

Thus, the dynamical conductivity of two-dimensional superconductors rises above the Higgs threshold with a modified power law $\sigma(\omega) \propto (\omega - m_H)^4$.

VII. DISCUSSION AND SUMMARY

In this work, we studied the critical dynamical properties of O(N)-symmetric models with relativistic dynamics in two space dimensions. In particular, we computed the line shape of the scalar susceptibility and the optical conductivity on either side of the quantum phase transition. Our results focus on properties that are universal in nature and are therefore relevant for many experimental realizations of quantum phase transitions.

We showed that the scalar susceptibility, in the ordered phase, contains a clear resonance at the Higgs mass m_H. By contrast, in the disordered phase the scalar susceptibility has a threshold at $\omega = 2\Delta$ with no conclusive evidence for a resonance above the threshold. In addition, we provide two universal dimensionless constants that characterize the dynamics: the ratio between the Higgs mass and the single-particle gap on mirror points across the transition, and the fidelity of the Higgs resonance. These predictions could be tested by future, high-resolution, experiments of the superfluid to Mott insulator transition in cold-atomic lattices.[7]

It is important to note that, close to the critical point, the scalar susceptibility captures the low-frequency behavior of a generic experimental probe that couples to the order-parameter amplitude and not to its direction.[10] We have also presented results for the optical conductivity on both sides of the phase transition. In both cases, we find a sharp rise of the spectral function at $\omega \approx 2\Delta$. The threshold frequency in the ordered phase can be associated with the Higgs mass m_H. This provides an independent estimate of the Higgs mass, one which agrees very well with the value obtained from the scalar susceptibility analysis. In addition, we have computed the high-frequency ($\omega \gg T$) universal conductance $\sigma_c^* = 0.3(\pm 0.1) \times \sigma_Q$. This value is in agreement with previous analytic calculations.[23] Unfortunately, the low-frequency ("hydrodynamic") limit $\omega \ll T$ is not accessible in the QMC simulation, as was discussed in Ref. 23.

We observe an approximate duality relation between the reactive components of the conductivity in both phases. The ordered (disordered) phase displays an inductive (capacitive) behavior, where the ratio C/L between the capacitance C and inductance L is found to be universal. To one-loop order, $C/L = 0.23\,\sigma_Q^2$. Furthermore, we show that the dual-vortex representation predicts an interesting physical interpretation to the admittance ratio $C/L = \rho_s \sigma_Q^2 / \rho_v$, where ρ_s is the superfluid stiffness and ρ_v is the vortex condensation density in the two phases. Both impedances can be computed directly from a Monte Carlo simulation without analytic continuation. We intend to do this in a future study. Finally, we have shown that for a charged system with Coulomb interaction, the power law of the spectral rise above the threshold changes from 2 to 4.

We hope that our results will motivate measurements of the optical conductivity in cold atoms by optical lattice phase modulation, as was suggested in Ref. 20. Such experiments could accurately measure the universal optical conductivity near the QCP and even the universal resistivity right at the critical point. Our analysis may also shed light on recent experiments on the superconductor to insulator transition in granular superconductors.[21] In this context, it will be interesting to extend these calculations to systems with varying degrees of disorder.

Note added. Recently, we learned of a few similar quantum Monte Carlo results,[38–40] all of which agree, within the error bars, with our estimate of the high-frequency conductivity at the critical point. We thank W. Witczak-Krempa for informing us of their work, and for some additional relevant references.

APEENDIX A: WORM ALGORITHM FOR O(N) MODELS

We present a QMC algorithm for O(N) lattice models [Eq. (12)]. The algorithm is based on the worm algorithm[24] extending it for general O($N > 2$) models. The first step is to expand Eq. (12) in strong coupling:

$$\mathcal{Z} = \int \mathcal{D}\vec{\phi} \prod_b \prod_\alpha \sum_{n_b^\alpha} \frac{1}{n_b^\alpha!} \left(\phi_{i_b}^\alpha \phi_{i_b'}^\alpha \right)^{n_b^\alpha} \prod_j e^{-V(|\vec{\phi}_j|^2)} \quad \text{(A1)}$$

with $\mathcal{D}\vec{\phi} \equiv \prod_i d^N \phi_i$. Here, $\{b\}$ represent the set of all lattice bonds, the site i_b is linked to the site i_b' through the bond b, the index $\alpha \in \{1, \ldots, N\}$ labels the N components of each $\vec{\phi}_i$, and $V(s) = \mu s + g s^2$ is the local onsite interaction. Next, we integrate out the fields $\vec{\phi}_i$. This can be achieved by noting that now the functional integral factorizes into a product of *single-site integrals*, such that

$$\mathcal{Z} = \sum_{\{n_b^\alpha\}} \prod_{b,\alpha} \frac{1}{n_b^\alpha!} \prod_i W(\{k_i^\alpha\}), \quad \text{(A2)}$$

where we define $k_i^\alpha = \sum_{b(i)}' n_b^\alpha$ as the sum over all bonds b emanating from site i. The single-site weight is then

$$W(\{k_i^\alpha\}) = \int d^N \phi_i \prod_\alpha \left(\phi_i^\alpha \right)^{k_i^\alpha} e^{-V(|\vec{\phi}|^2)}. \quad \text{(A3)}$$

We may write

$$W(\{k_i^\alpha\}) = \int d^N \phi_i \int_0^\infty ds\, e^{-V(s)} \delta(s - |\vec{\phi}_i|^2) \prod_\alpha \left(\phi_i^\alpha \right)^{k_i^\alpha}$$

$$= \frac{1}{2\pi} \int_0^\infty ds\, e^{-V(s)} \int_{-\infty}^\infty d\lambda\, e^{i\lambda s} \prod_\alpha \mathcal{I}(k_i^\alpha), \quad \text{(A4)}$$

where

$$\mathcal{I}(k_i^\alpha) = \int_{-\infty}^\infty d\phi_i^\alpha\, e^{-i\lambda(\phi_i^\alpha)^2} \left(\phi_i^\alpha \right)^{k_i^\alpha}$$

$$= (i\lambda)^{-(k_i^\alpha+1)/2} \, \Gamma\left(\frac{1}{2} + \frac{1}{2} k_i^\alpha \right) \delta_{k_i^\alpha, \text{even}}. \quad \text{(A5)}$$

We now encounter the integral

$$\int_{-\infty}^{\infty} d\lambda\, e^{i\lambda s} (i\lambda)^{-J} = 2\, s^{J-1}\, \Gamma(1-J)\, \sin(\pi J), \quad \text{(A6)}$$

where $J = \frac{1}{2}(N + K_i)$ and $K_i = \sum_\alpha k_i^\alpha$. The above integral converges only if $0 < \mathrm{Re}\, J < 1$, however, our initial expression in Eq. (A3) is clearly convergent for all possible values of J, which licenses us to analytically continue the above expression, using the identity $\Gamma(J)\,\Gamma(1-J) = \pi/\sin(\pi J)$. We then obtain

$$W(\{k_i^\alpha\}) = Q\left(\frac{1}{2}N + \frac{1}{2}K_i\right) \prod_\alpha \Gamma\left(\frac{1}{2} + \frac{1}{2}k_i^\alpha\right) \delta_{k_i^\alpha,\mathrm{even}}$$
$$\text{(A7)}$$

with

$$Q(J) = \frac{1}{\Gamma(J)} \int_0^\infty ds\, e^{-V(s)}\, s^{J-1}. \quad \text{(A8)}$$

The one-dimensional integrals $Q(J)$ can be evaluated numerically to high precision and tabulated prior to the QMC simulation. In this representation, the partition function sum runs over all integer values of the bond's strength n_b^α, replacing the $\vec{\phi}_i$ field integrations. The sum is restricted only to closed-path loops due to constraint $\delta_{k_i^\alpha,\mathrm{even}}$.

The updating procedure closely follows the worm algorithm, considering an extended partition function

$$\mathcal{Z}_G = \sum_{i,j} \langle \phi_i^\alpha \phi_j^\alpha \rangle. \quad \text{(A9)}$$

The field's insertion $\phi_i^\alpha \phi_j^\alpha$ breaks the closed-path condition by adding a single open loop. The open loop's head is located at i and its tail at j.

For simplicity, we choose the open loop to be one of the flavors α. The updating procedure consists of two elementary steps. The first move is a shift move in which we move the worm's head to one of the neighboring sites connected with the bond b. During the move, we either increase or decrease the bond's strength n_b^α. The second move is a jump move, which is relevant only for closed loops where the head and the tail are located in the same site. We choose one of the lattice sites and jump with the head tail pair to that site. The QMC acceptance ratios can be easily derived from Eqs. (A7) and (A2) similarly to the argument in Ref. 24. We tested the correctness of our numerical implementation by comparing with previous QMC simulation and to analytic results of the Gaussian model limit of Eq. (12) ($g = 0$). The results agree within the statistical errors.

We also provide an explicit expression for the sampling of the scalar susceptibility in the closed-path representation. The operator insertion $\vec{\phi}_i^2$ effectively introduces a factor of s to the integrand in Eq. (A4), in which case Eq. (A8) is replaced by $J_i\, Q(J_i + 1)$. Inserting $(\vec{\phi}_i^2)^2$ introduces a factor of s^2 and results in $J_i(J_i + 1)\, Q(J_i + 2)$. Thus, the insertion $\vec{\phi}_i^2 \vec{\phi}_j^2$ yields

$$\langle \vec{\phi}_i^2 \vec{\phi}_j^2 \rangle = \left\langle \frac{J_i J_j\, Q(J_i + 1)\, Q(J_j + 1)}{Q(J_i)\, Q(J_j)} \right\rangle \quad (i \neq j)$$

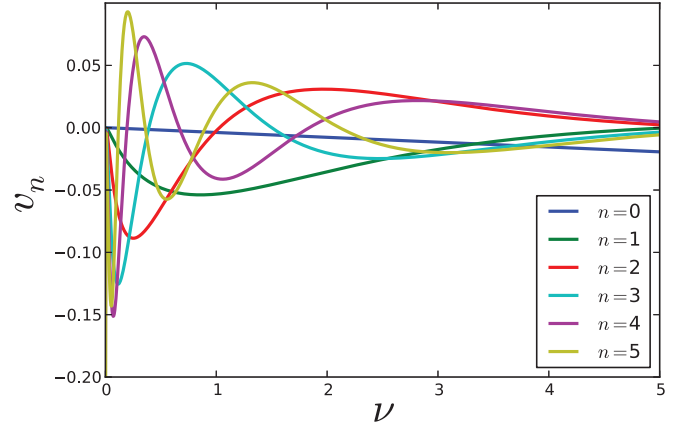$$= \left\langle \frac{J_i(J_i + 1)\, Q(J_i + 2)}{Q(J_i)} \right\rangle \quad (i = j). \quad \text{(A10)}$$

FIG. 13. (Color online) The first five vectors $v_n(\nu)$ corresponding to the largest singular values in W.

APPENDIX B: ANALYTIC CONTINUATION OF IMAGINARY-TIME QMC DATA

1. General formulation

We use imaginary-time action (12) in the QMC simulations in order for the QMC weights to be real and positive, avoiding the dynamical sign problem. The real frequency, dissipative response function $A(\nu)$ can be obtained by numerical analytic continuation,[41] which amounts to inverting the equation

$$\mathcal{G}(i\omega_m) = \int_0^\infty \frac{d\nu}{\pi} \frac{2\nu}{\omega_m^2 + \nu^2}\, A(\nu). \quad \text{(B1)}$$

The kernel

$$K(m,\nu) = \frac{1}{\pi} \frac{2\nu}{\omega_m^2 + \nu^2} \quad \text{(B2)}$$

needs to be inverted in order to formally obtain

$$A(\nu) = K^{-1} \mathcal{G}(i\omega_m). \quad \text{(B3)}$$

Unfortunately, K is an ill-conditioned operator. The inversion is extremely sensitive to inevitable statistical noise in $\mathcal{G}$.

The stability of the inversion problem can be analyzed by the singular value decomposition (SVD)

$$K = U W V^T, \quad \text{(B4)}$$

where U and V are unitary matrices whose rows are the eigenvectors $\langle u_n|$ and $\langle v_n|$. The first five eigenvectors $v_n(\nu)$ are plotted in Fig. 13. W is diagonal with real, non-negative SVD eigenvalues w_n. These are plotted on a logarithmic scale as a function of n in Fig. 14. W has up to $\mathcal{N}$ nonzero singular values, where $\mathcal{N}$ is the number of QMC data points.

From Eq. (B4), the pseudoinversion of K is given by

$$\bar{K}^{-1} = V \bar{W}^{-1} U^T. \quad \text{(B5)}$$

Here, $\bar{W}$ is a square diagonal matrix which contains only the nonzero eigenvalues $w_n \neq 0$.
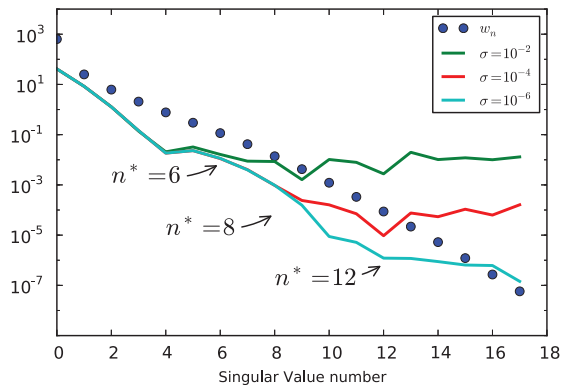
FIG. 14. (Color online) SVD analysis of the numerical analytical continuation. n labels the SVD eigenmodes. The filled circles are the rapidly decreasing SVD eigenvalues of K, denoted w_n. Magnitudes of projections of noisy data, for the test model [Eq. (B13)], are denoted by $|\tilde{p}_n|$. σ is the variance of the artificial noise added to the Matsubara data. The breakpoints n^* denote the mode index where noise dominates the signal, and the projections start to flatten. The values of n^* increase when the noise level decreases.

The SVD eigenvalues w_n can be calculated by diagonalizing the Hermitian matrix $(KK^\dagger)_{ij}$:

$$(KK^\dagger)_{ij} = \int_{-\infty}^{\infty} \frac{d\omega}{2\pi} \frac{\omega^2}{(\omega_i^2 + \omega^2)(\omega_j^2 + \omega^2)}$$
$$= \frac{1}{2(|\omega_i| + |\omega_j|)} = \frac{\beta}{4\pi} \frac{1}{|i| + |j|}. \quad (B6)$$

Since $\mathcal{G}(\tau)$ is real, $\mathcal{G}_n = \mathcal{G}_{-n}$, and by projecting out the zero mode, we may restrict both i and j to be positive integers in Eq. (B6).

Matrices of the form

$$H_{ij}(\tau,\theta) = \frac{\tau^{i+j}}{i+j+\theta}, \quad (i,j) \in \{0,\ldots,N\} \quad (B7)$$

are known as Hilbert matrices. We are interested in the case of $\tau = 1$ and $\theta = 2$. An exact bound on the dependence of the smallest eigenvalue on the matrix size was obtained by Ref. 42:

$$w_{\min}^{(N)} \sim \kappa \sqrt{N} (1+\sqrt{2})^{-4N}[1+o(1)],$$
$$\ln(w_{\min}^{(N)}) \sim -3.525\,49\,N + 0.5\ln N + 0.7909, \quad (B8)$$

with

$$\kappa = \frac{2^{15/4}\pi^{3/2}}{(1+\sqrt{2})^4} = 2.205\,385\cdots. \quad (B9)$$

As we see, the minimal eigenvalue decreases faster than exponentially with N, which is consistent with the behavior found numerically in Fig. 14.

2. Pseudoinversion by truncated SVD

In practice, the noisy QMC data, called $\tilde{\mathcal{G}}$, can be decomposed as

$$\tilde{\mathcal{G}} = \mathcal{G}^{\text{sig}} + \xi, \quad (B10)$$

where $\mathcal{G}^{\text{sig}}$ is the true signal, and ξ is a random noise. The noise interferes with the numerical inversion of $\mathcal{G}^{\text{sig}}$. To see

this, the data $\tilde{\mathcal{G}}$ are projected onto the eigenvectors u_n, which yields the real numbers

$$\tilde{p}_n = \langle u_n|\tilde{\mathcal{G}}\rangle = \langle u_n|\mathcal{G}^{\text{sig}}\rangle + \langle u_n|\xi\rangle$$
$$\equiv p_n^{\text{sig}} + \xi_n. \quad (B11)$$

The pseudoinversion (B5) yields

$$A(\nu) = \sum_n \frac{\tilde{p}_n}{w_n} v_n(\nu) = \sum_n \left(\frac{p_n^{\text{sig}}}{w_n} v_n(\nu) + \frac{\xi_n}{w_n} v_n(\nu) \right). \quad (B12)$$

Since $\mathcal{G}^{\text{sig}}$ is the analytic continuation of a normalizable function, $\sum_n |p_n^{\text{sig}}/w_n|^2$ must converge. This implies that $|p_n^{\text{sig}}| < w_n$ at large n. On the other hand, ξ_n is not the analytic continuation of a normalizable function, and therefore is not necessarily bounded by w_n. For white noise, ξ_n are random numbers whose variance is independent on n.

Therefore, one can readily identify a *breakpoint* n^*, which for $n < n^*$, $\tilde{p}_n \approx p_n^{\text{sig}}$, and for $n > n^*$, $\tilde{p}_n \approx \xi_n$. The breakpoint serves to truncate the inversion and eliminate the dominance of noise terms. It can also allow an estimate of the truncation error.

Let us illustrate this procedure by a test model

$$A^{\text{model}}(\nu) = \nu^3 (e^{-(\nu-\Delta)^2} + e^{-(\nu+\Delta)^2}). \quad (B13)$$

In Fig. 14 we present the projections to the u_n basis of the test model in Eq. (B13). w_n and $|p_n^{\text{sig}}|$ rapidly decay, as expected from the Riemann-Lebesgue lemma for a smooth spectral function. We add an artificial white noise with increasing variance σ. As expected, the (approximately) exponential decay of $\tilde{p}_n$ stops abruptly at n^*, where $|\tilde{p}_{n^*}| \approx |\xi_{n^*}|$.

As seen in Fig. 14, the breakpoints n^* are chosen where the curves average slope flattens abruptly. n^* increase as the noise is reduced.

A truncated SVD inversion provides a controlled approximation for the spectral function:

$$\tilde{A}^{\text{SVD}}(\nu) \simeq \sum_{n=1}^{n_{\text{SVD}}} \frac{\tilde{p}_n}{w_n} v_n(\nu). \quad (B14)$$

The modes higher than n_{SVD} are discarded because their coefficients (which only contribute random noise to the spectral function) blow up exponentially with n. If we know the bound on the signal's convergence rate $|p^{\text{sig}}/w_n|^2 < ce^{-\alpha n}$, we can estimate the error in the norm as

$$||\delta\tilde{A}||^2 = \sum_{n=n_{\text{SVD}}+1}^{\mathcal{N}} \left| \frac{p_n^{\text{sig}}}{w_n} \right|^2 < \frac{\tilde{p}_{n_{\text{SVD}}}^2}{\alpha w_{n_{\text{SVD}}}^2}. \quad (B15)$$

Thus, the smaller the noise level, the larger n_{SVD} and therefore the smaller the error in the spectral function [Eq. (B15)].

In Fig. 15, we show the SVD analysis of the QMC data for the real O(2) model. The projections $\tilde{p}_n$ flatten roughly at $n^* \approx 11$, as they behave in the test model in Fig. 14.

$\tilde{A}^{\text{SVD}}$ can exhibit spurious oscillations due to the missing modes $\{v_n(\nu), n > n_{\text{SVD}}\}$. This effect, which is part of the error $||\delta\tilde{A}||^2$, is similar to spurious oscillations obtained by a truncated inverse Fourier transform. In cases where it is known that $A(\nu) > 0$ (as for the scalar susceptibility and
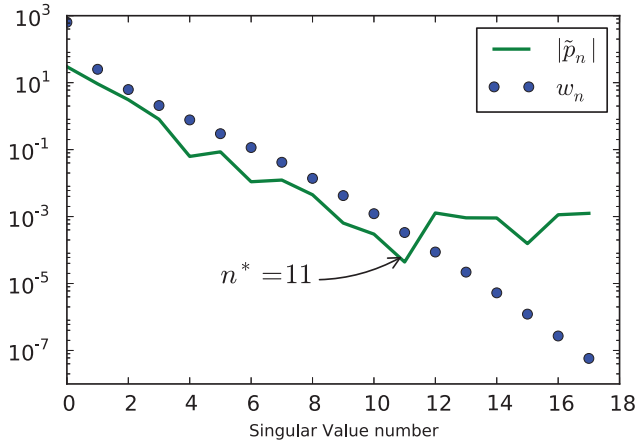
FIG. 15. (Color online) Comparison between the projections p_n (solid lines) and the singular values of the kernel w_n (circles) for the high-quality QMC data for the O(2) model. The linear system size is $L = 120$, and coupling constant is $\delta g = 1.17\%$. We see that due to the effect of the noise, $\tilde{p}_n$ flattens at the breakpoint at $n^* \approx 11$.

real conductivity), the SVD truncation can produce unsightly negative regions.

In Fig. 16, we plot the $\tilde{A}^{\text{SVD}}(\nu)$ for increasing values of n_{SVD}. We see that indeed the reconstructed solution converges as we increase n and remains stable up to $n \approx 11$, which is where we locate the breakpoint in the SVD analysis. For $n = 12$, the inverted errors dominate the spectral function, which yields a wildly erroneous result.

3. Maximum entropy and other regularizations

The QMC simulation produces noisy variables $\mathcal{G}(i\omega_m)$, whose covariance matrix is defined as

$$\Sigma^{-1} = \langle \mathcal{G}(i\omega_m)\,\mathcal{G}(i\omega_n) \rangle. \tag{B16}$$

A condition for the inverted spectral function is that

$$\chi^2 = (\mathcal{G} - KA)^T \, \Sigma \, (\mathcal{G} - KA) \approx \mathcal{N}, \tag{B17}$$

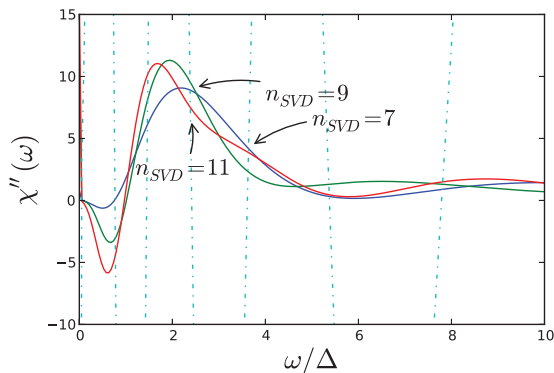where $\mathcal{N}$ is the number of data points.

FIG. 16. (Color online) Analytic continuation obtained from the first n singular values, for the QMC data of Fig. 15. We see that spectral functions converge to until $n \leqslant 11$, in agreement with assigning $n^* = 11$ where $\tilde{p}_n$ starts to flatten in Fig. 15. For $n_{\text{SVD}} = 12$ (dashed line), the condition $\tilde{p}_n < w_n$ is violated, and the resulting spectral function wildly differs from the converged function since it is dominated by random amplified errors.

As we have seen before, since K has very small SVD eigenvalues, there is a large family of functions $A(\nu)$ which have the same $\chi^2/\mathcal{N} \approx 1$. The SVD truncation is one way to choose among these functions, but the result may have spurious oscillations, and turn negative in some regions. To improve on this approximation, one needs to impose extra conditions on $A(\nu)$, which amounts to extrapolation of Eq. (B14) to include higher SVD modes. A common approach, which ensures positivity, is to introduce a cost functional $f(A)$, and to variationally minimize

$$Q = \tfrac{1}{2}\chi^2 + \lambda f(A) \tag{B18}$$

with respect to A. This minimization lifts the degeneracy in χ^2, and depends critically on the choice of λ. λ can be chosen by the L-curve method,[43] which is analogous to the determination of the breakpoint n^* described above.

Two cost functions are commonly used: (1) the "maximum entropy" (MaxEnt),[41]

$$f^{\text{MaxEnt}}(A) = -\sum_i A(\nu_i)\ln A(\nu_i), \tag{B19}$$

which is based on a Bayesian statistics, and (2) the "Laplacian"

$$f^{\text{Lap}}(A) = \sum_i \left.\frac{d^2A(\nu)}{d\nu^2}\right|_{\nu=\nu_i}, \tag{B20}$$

which penalizes unsmooth spectral functions (or long real-time decay). In these functionals, the real frequency ν is discretized as a finite sequence ν_i.

A different strategy is the stochastic regularization.[44,45] In this method, the spectral function is obtained by averaging over a large sample of randomly chosen solutions consistent with $\chi^2/\mathcal{N} \approx 1$. First, a random positive spectral function is generated. Then, the goodness of fit is minimized using the steepest-descent method while imposing positivity at each step. This procedure is repeated until $\chi^2/\mathcal{N} \approx 1$. Averaging over the random initial conditions leads to the final spectral function.

A complementary approach is to estimate the pole structure of $A(\nu)$, using a Padé approximation. $\tilde{\mathcal{G}}$ is fitted to a rational function

$$\tilde{\mathcal{G}}(i\omega_m) = P_{n_p}(i\omega_m)/Q_{n_p}(i\omega_m), \tag{B21}$$

where P_{n_p} and Q_{n_p} are polynomials of order n_p. Since $\tilde{\mathcal{G}}$ is an analytic function of $i\omega_m$, we can perform the analytic continuation explicitly by taking $\tilde{A}(\omega) = \text{Im}\tilde{\mathcal{G}}(i\omega_m \to \omega + i0^+)$. For the best inversion, one can increase the value of n_p until $\chi^2/\mathcal{N} \approx 1$. Further increase of n_p leads to overfitting and the appearance of spurious poles. n_p needs to be determined, with similar considerations to those determining n_{SVD}.

In Fig. 17, we show a comparison of the different regularization approaches for the same QMC data as used in Fig. 16. We note that the position of the Higgs peak varies only slightly between different analytic continuation methods, but functions differ somewhat in the higher-frequency structure.

As a final note, we comment on the form for the kernel $K(i\omega, \nu)$ for QMC simulation with discretized imaginary-time axis. In this case, the imaginary-time axis gets a discrete set of values $\tau_i = \Delta\tau \times i$ with $i \in \{0, \ldots, M-1\}$ with $\Delta\tau = \beta/M$. The corresponding Matsubara frequencies are $\omega_m = 2\pi n/\beta$
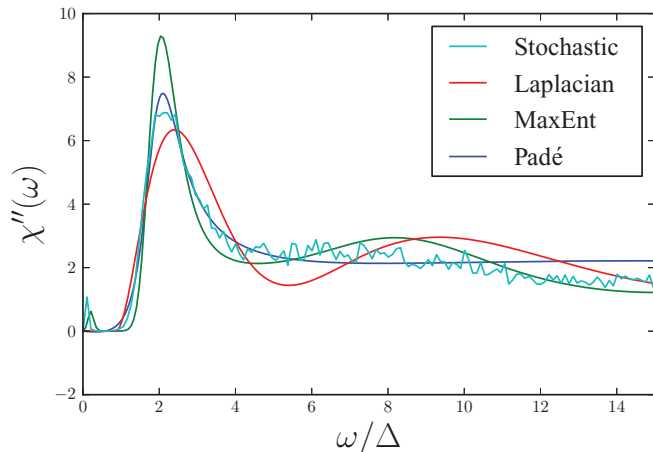
FIG. 17. (Color online) Comparison of different regularization methods. Note that the Higgs peak position varies only slightly between the different methods, described in Sec. B 3.

with $m \in \{0, \ldots, M-1\}$. The kernel is given by a sum over all aliases of the original kernel:

$$\tilde{K}(i\omega_m, \nu) = \frac{1}{\pi} \sum_{k=-\infty}^{\infty} \frac{2\nu}{[2\pi(n+Mk)/\beta]^2 + \nu^2}$$

$$= \frac{\beta}{M\pi} \frac{\sinh(\beta\nu/M)}{\cosh(\beta\nu/M) - \cos(2\pi m/M)}. \quad (B22)$$

4. Spherical averaging

A desirable feature of Eq. (1) and its discretized approximation (12) is the Euclidean space-time symmetry. As a consequence, it is not necessary to single out any one specific direction as the "time" direction. In particular, ignoring weak anisotropies arising from the underlying cubic lattice, correlation functions such as those in Eq. (13) are spherically symmetric and only depend on the Euclidean distance from the point $\mathbf{r} = (\tau, x, y)$ to the origin. This is especially correct near the QCP, where the large correlation length ensures that the correlation function at long distances is insensitive to the discrete nature of the lattice.

This observation suggests that one may reduce the statistical noise by performing a spherical average over all possible time directions. In this method, the correlation function at time τ is obtained by averaging over all the points within a thin spherical shell between radius $r = \tau$ and $r = \tau + \delta\tau$. This leads to a large enhancement in statistics: for a $L \times L \times L$ system, $\mathcal{O}(L^3)$ data points are used instead of the $\mathcal{O}(L)$ points typically used in computing the correlation function. In order to implement this method accurately, it is necessary to account for the weak anisotropy arising from the underlying cubic lattice. This is done by projecting out the lowest cubic anisotropies prior to the averaging.

The bulk of the data presented in this paper were obtained by averaging over the three principal axes only, and not taking advantage of the full spherical averaging. However, preliminary numerical tests show that spherical averaging does indeed yield high-quality results while requiring shorter simulations. This effect may be significant in light of the high

sensitivity of numerical analytic continuation to noise. We intend to develop this strategy further in future work.

APPENDIX C: COMPLEX CONDUCTIVITY

In this section, we will derive the complex conductivity for the disordered and ordered phases in weak coupling. To one-loop order, the paramagnetic response in the disordered phase is given by[23]

$$\Pi_{xx}^{\mathrm{P}}(p) = \int \frac{d^3q}{(2\pi)^3} \frac{4q_x^2}{q^2 + \Delta^2} \frac{1}{(q+p)^2 + \Delta^2}, \quad (C1)$$

where Δ is the renormalized single-particle gap in the disordered phase and $p = (\omega_m, 0, 0)$. Introducing the Feynman parameter x and shifting $q \rightarrow q - xp$,

$$\Pi_{xx}^{\mathrm{P}}(p) = \int_0^1 dx \int \frac{d^3q}{(2\pi)^3} \frac{4q_x^2}{[q^2 + x(1-x)p^2 + \Delta^2]^2}. \quad (C2)$$

Performing the q integration up to a cutoff Λ, we obtain

$$\Pi_{xx}^{\mathrm{P}}(p) = \frac{2}{3\pi^2} \int_0^1 dx \left[\Lambda - \frac{3\pi}{4} \sqrt{p^2 x(1-x) + \Delta^2} \right] \quad (C3)$$

up to corrections that vanish as $\Lambda \rightarrow \infty$. To obtain the full response, we must subtract the diamagnetic part. Since the superfluid stiffness vanishes in the disordered phase, this is given by $\Pi_{xx}^{\mathrm{D}} = \Pi_{xx}^{\mathrm{P}}(p \rightarrow 0)$. This cancels the linearly divergent term, to yield

$$\Pi_{xx}(p) = -\frac{1}{2\pi} \int_0^1 dx \left[\sqrt{p^2 x(1-x) + \Delta^2} - \Delta \right] \quad (C4)$$

$$= \frac{\Delta}{4\pi} - i \frac{4\Delta^2 + p^2}{16\pi p} \ln\left(\frac{2\Delta - ip}{2\Delta + ip} \right). \quad (C5)$$

We analytically continue by taking $p \rightarrow -i\omega + \epsilon$, resulting in

$$\Pi_{xx}(\omega) = \frac{\Delta}{4\pi} + \frac{4\Delta^2 - \omega^2}{16\pi\omega} \ln\left(\frac{2\Delta - \omega - i\epsilon}{2\Delta + \omega + i\epsilon} \right). \quad (C6)$$

The conductivity is then

$$\sigma(\omega) = \frac{1}{i\omega} \Pi_{xx}(\omega) = \mathrm{Re}\sigma(\omega) + i\mathrm{Im}\sigma(\omega)$$

$$= \frac{1}{\omega} \mathrm{Im}\Pi_{xx}(\omega) - \frac{i}{\omega} \mathrm{Re}\Pi_{xx}(\omega). \quad (C7)$$

We note that $\mathrm{Re}\sigma(\omega)$ vanishes for $\omega < 2\Delta$. Above the threshold, we obtain

$$\mathrm{Re}\sigma(\omega) = \frac{\omega^2 - 4\Delta^2}{16\omega^2} \qquad (\omega > 2\Delta). \quad (C8)$$

The imaginary part is given by

$$\mathrm{Im}\sigma(\omega) = \frac{1}{16\pi\omega^2} \left[(4\Delta^2 - \omega^2) \ln\left| \frac{2\Delta - \omega}{2\Delta + \omega} \right| + 4\Delta\omega \right]. \quad (C9)$$

In the ordered phase, the paramagnetic response is given by[5,6]

$$\Pi_{xx}^{\mathrm{P}}(p) = \int \frac{d^3q}{(2\pi)^3} \frac{4q_x^2}{q^2 + m^2} \frac{1}{(q+p)^2}. \quad (C10)$$

Here, m is the Higgs mass. As before, we introduce the Feynman parameter x and shift $q \to q - xp$:

$$\Pi^{\mathrm{P}}_{xx}(p) = \int_0^1 dx \int \frac{d^3q}{(2\pi)^3}$$
$$\times \frac{4q_x^2}{[q^2 + (1-x)(xp^2 + m^2)]^2}. \quad \text{(C11)}$$

Performing the q integration, we obtain

$$\Pi_{xx}(p) = \rho_s + \frac{m(3m^2 + 5p^2)}{24\pi p^2} - i\frac{(p^2+m^2)^2}{16\pi p^3} \ln\left(\frac{m-ip}{m+ip}\right). \quad \text{(C12)}$$

In the final expression, we absorbed the constant term (including the linear divergence) and the diamagnetic contribution into the superfluid stiffness ρ_s.

After analytic continuation, the real conductivity is given by

$$\mathrm{Re}\,\sigma(\omega) = \pi\rho_s\delta(\omega) + \frac{(\omega^2 - m^2)^2}{16\omega^4}\Theta(\omega - m), \quad \text{(C13)}$$

with ρ_s being the superfluid stiffness. The imaginary part of the conductivity is

$$\mathrm{Im}\,\sigma(\omega) = \frac{\rho_s}{\omega} + \frac{(m^2-\omega^2)^2}{16\pi\omega^4}\ln\left|\frac{m-\omega}{m+\omega}\right|$$
$$+ \frac{m(3m^2 - 5\omega^2)}{24\pi\omega^3}. \quad \text{(C14)}$$

---

[1] M. P. A. Fisher, P. B. Weichman, G. Grinstein, and D. S. Fisher, Phys. Rev. B **40**, 546 (1989).

[2] S. Chakravarty, B. I. Halperin, and D. R. Nelson, Phys. Rev. B **39**, 2344 (1989).

[3] S. D. Huber, B. Theiler, E. Altman, and G. Blatter, Phys. Rev. Lett. **100**, 050404 (2008).

[4] S. Sachdev, *Quantum Phase Transitions*, 2nd ed. (Cambridge University Press, New York, 2011).

[5] D. Podolsky, A. Auerbach, and D. P. Arovas, Phys. Rev. B **84**, 174522 (2011).

[6] N. H. Lindner and A. Auerbach, Phys. Rev. B **81**, 054512 (2010).

[7] M. Endres, T. Fukuhara, D. Pekker, M. Cheneau, P. Schau, C. Gross, E. Demler, S. Kuhr, and I. Bloch, Nature (London) **487**, 454 (2012).

[8] D. Podolsky and S. Sachdev, Phys. Rev. B **86**, 054508 (2012).

[9] L. Pollet and N. Prokof'ev, Phys. Rev. Lett. **109**, 010401 (2012).

[10] S. Gazit, D. Podolsky, and A. Auerbach, Phys. Rev. Lett. **110**, 140401 (2013).

[11] K. Chen, L. Liu, Y. Deng, L. Pollet, and N. Prokof'ev, Phys. Rev. Lett. **110**, 170403 (2013).

[12] M. P. A. Fisher and D. H. Lee, Phys. Rev. B **39**, 2756 (1989).

[13] J. Demsar, K. Biljaković, and D. Mihailovic, Phys. Rev. Lett. **83**, 800 (1999).

[14] R. Yusupov, T. Mertelj, V. V. Kabanov, S. Brazovskii, P. Kusar, J.-H. Chu, I. R. Fisher, and D. Mihailovic, Nat. Phys. **6**, 681 (2010).

[15] K. B. Lyons, P. A. Fleury, J. P. Remeika, A. S. Cooper, and T. J. Negran, Phys. Rev. B **37**, 2353 (1988).

[16] J. B. Parkinson, J. Phys. C: Solid State Phys. **2**, 2003 (1969).

[17] P. A. Fleury and H. J. Guggenheim, Phys. Rev. Lett. **24**, 1346 (1970).

[18] R. J. Elliott and M. F. Thorpe, J. Phys. C: Solid State Phys. **2**, 1630 (1969).

[19] B. S. Shastry and B. I. Shraiman, Phys. Rev. Lett. **65**, 1068 (1990).

[20] A. Tokuno and T. Giamarchi, Phys. Rev. Lett. **106**, 205301 (2011).

[21] D. Sherman, B. Gorshunov, S. Poran, J. Jesudasan, P. Raychaudhuri, N. Trivedi, M. Dressel, and A. Frydman, arXiv:1304.7087.

[22] M. P. A. Fisher, G. Grinstein, and S. M. Girvin, Phys. Rev. Lett. **64**, 587 (1990).

[23] K. Damle and S. Sachdev, Phys. Rev. B **56**, 8714 (1997).

[24] N. Prokof'ev and B. Svistunov, Phys. Rev. Lett. **87**, 160601 (2001).

[25] M. Hasenbusch, J. Phys. A: Math. Gen. **34**, 8221 (2001).

[26] M. Hasenbusch and T. Török, J. Phys. A: Math. Gen. **32**, 6361 (1999).

[27] J. Šmakov and E. Sørensen, Phys. Rev. Lett. **95**, 180603 (2005).

[28] B. Capogrosso-Sansone, S. G. Söyler, N. Prokof'ev, and B. Svistunov, Phys. Rev. A **77**, 015602 (2008).

[29] A. Rançon, O. Kodio, N. Dupuis, and P. Lecheminant, Phys. Rev. E **88**, 012113 (2013).

[30] K. Beach, arXiv:cond-mat/0403055.

[31] S. Sachdev, Phys. Rev. B **59**, 14054 (1999).

[32] A. Milchev, K. Binder, and D. Heermann, Z. Phys. B **63**, 521 (1986).

[33] M.-C. Cha, M. P. A. Fisher, S. M. Girvin, M. Wallin, and A. P. Young, Phys. Rev. B **44**, 6883 (1991).

[34] There is ambiguity in the literature regarding the sign convention of the reactive part of the optical conductivity. Here, positive/negative values reflect inductive/capacitive behavior. This is opposite to the convention often used in electric circuits.

[35] M. Stone and P. R. Thomas, Phys. Rev. Lett. **41**, 351 (1978).

[36] D. P. Arovas and J. A. Freire, Phys. Rev. B **55**, 1068 (1997).

[37] A. Mihlin and A. Auerbach, Phys. Rev. B **80**, 134521 (2009).

[38] W. Witczak-Krempa, E. Sorensen, and S. Sachdev, arXiv:1309.2941.

[39] K. Chen, L. Liu, Y. Deng, L. Pollet, and N. Prokof'ev, arXiv:1309.5635.

[40] M. Swanson, Y. L. Loh, M. Randeria, and N. Trivedi, arXiv:1310.1073.

[41] M. Jarrell and J. Gubernatis, Phys. Rep. **269**, 133 (1996).

[42] G. A. Kalyabin, Funct. Anal. Appl. **35**, 67 (2001).

[43] P. C. Hansen and D. P. O'Leary, SIAM J. Sci. Comput. **14**, 1487 (1993).

[44] A. S. Mishchenko, N. V. Prokof'ev, A. Sakamoto, and B. V. Svistunov, Phys. Rev. B **62**, 6317 (2000).

[45] A. W. Sandvik, Phys. Rev. B **57**, 10287 (1998).